Simple embedding scheme for the spectral properties of the Single-Impurity Anderson Model

Soumyodipto Mukherjee and David R. Reichman
Department of Chemistry, Columbia University, New York, NY, 10027, USA

In this work we outline a simple and numerically inexpensive approach to describe the spectral features of the single-impurity Anderson model. The method combines aspects of the density matrix embedding theory (DMET) approach with a spectral broadening approach inspired by those used in numerical renormalization group (NRG) methods. At zero temperature for a wide range of U, the spectral function produced by this approach is found to be in good agreement with general expectations as well as more advanced and complex numerical methods such as DMRG-based schemes. The theory developed here is simply transferable to more complex impurity problems.

arXiv:1611.04521v2 [cond-mat.str-el] 28 Nov 2016

I. INTRODUCTION

Quantum impurity models play a major role in modern condensed matter physics. As proxies of physical reality, impurity models encapsulate complex physical behavior within the simple framework of a small subsystem hybridized with an otherwise noninteracting bath. Such models have laid the foundation for our understanding of qualitative phenomena such as quantum dissipation, namely the generic features of how a bath induces dephasing and relaxation in a small subsystem, as well as detailed specific and quantitative phenomena such as the description of magnetic impurities in metals and the relaxation of tunneling centers in low-temperature dielectric media[1]. Due to central role played by impurity problems in condensed matter physics, the development of methods for the the accurate description of their properties, in particular their real-time or real-frequency behavior, remains at the forefront of the field.

One of the most important and well-studied impurity models is the Anderson model[2]. The Anderson Hamiltonian describes an electron-correlated quantum dot hybridized with a non-interacting bath of fermions. The physics of the Anderson model subsumes that of the Kondo model, and thus describes the physics of dilute magnetic impurities in metals, including the appearance of a resistivity minimum and the eventual formation of a $T = 0$ singlet state induced by the complete screening of the impurity spin by the conduction electrons[3]. In the context of strongly correlated solids, the Anderson model has taken on renewed importance with the development of dynamical mean-field theory (DMFT)[4–6], a quantum embedding approach where Hubbard-like models[7–9] are self-consistently mapped to Anderson-like impurity problems. In this latter regard, the Anderson model and its variants provide a window into the properties of wide range of strongly correlated materials.

DMFT is a Green's function-based approach which requires the solution of the spectral function of the Anderson model on the real-frequency axis. Despite the reduction of complexity afforded by the mapping from the Hubbard model to the Anderson model, the determination of real-time or real-frequency spectral behavior is a difficult task. Simple quasi-analytical approaches like the non-crossing approximation[10–12] are often not sufficiently accurate in the most interesting physical regimes[13]. Analytic continuation of exact imaginary-time quantum Monte Carlo data is an unstable numerical problem which can often produce artifacts[14–17], while exact diagonalization is restricted to a small number of bath states, rendering a detailed accurate description of realistic DMFT problems difficult or out of reach[17].

Recently great progress has been made in the formulation and use of time dependent density matrix renormalization group (DMRG) and related approaches[18, 19], as well as sophisticated renormalization group approaches to study the behavior of the Anderson model on the real time and frequency axis[20–24]. These matrix product-based methods have been used as impurity solvers in one and multi-orbial DMFT calculations to obtain spectral functions of the one and two-band Hubbard models [25–27]. These approaches are expected to be quite accurate, but may have some difficulty properly resolving, for example, the high frequency behavior of the spectral function. Such techniques, while powerful, are also theoretically and numerically involved.

In this work we propose a different and extremely simple method for the calculation of the real-frequency spectral function of the Anderson model. The approach combines the use a density-matrix embedding theory (DMET) -like decomposition without self consistency[28–33] with a simple and physical protocol motivated by some implementations of the numerical renormalization group (NRG) for assigning line widths[20, 34]. The results are compatible with those produced by far more sophisticated theoretically and numerically involved approaches. In principle the method outlined here is extendable to more complex situations such as those that arise in cluster DMFT where the embedded impurity-like system contains multiple sites or orbitals.

The paper is organized as follows: In Sec.II we introduce the single-impurity Anderson model (SIAM) and briefly discuss the ground state embedding approach and the calculation of $T = 0$ spectral functions. We propose a way to obtain the peak spectrum and a frequency-dependent broadening scheme is employed that generates smooth spectral functions. Sec.III A compares the ground state and spectral properties of a finite-sized

SIAM to numerically exact results. In Sec.III B we analyze the spectral properties for the bulk case. Sec.IV is devoted to our concluding remarks.

II. BACKGROUND AND METHODOLOGY

A. Model and embedding approach

The single-impurity Anderson model (SIAM)[2] describes a single interacting impurity coupled to a host conduction band of noninteracting fermionic levels. The Hamiltonian reads

$$\begin{aligned}\hat{H} &= \hat{H}_{\rm cb} + \hat{H}_{\rm imp} + \hat{H}_{\rm hyb} \\ &= \sum_{k\sigma} \epsilon_k \hat{n}_{k\sigma} + \sum_{\sigma} \left(\epsilon_d + \frac{U}{2} \hat{n}_{d-\sigma} \right) \hat{n}_{d\sigma} \\ &\quad + \sum_{k\sigma} V_k (c^\dagger_{d\sigma} c_{k\sigma} + c^\dagger_{k\sigma} c_{d\sigma}) \ , \end{aligned} \tag{1}$$

where ϵ_k denotes the energy levels of the conduction band, ϵ_d the impurity level, U the interaction on the impurity, $\hat{n}_{d\sigma} = c^\dagger_{d\sigma} c_{d\sigma}$ is the occupancy of the impurity, $\hat{n}_{k\sigma} = c^\dagger_{k\sigma} c_{k\sigma}$ is the band occupancy and V_k the hybridization between the impurity and the conduction band. At this stage we defer the discussion of the choice of the hybridization parameter until later to keep the discussion general.

The approach we employ is based on a simplified version of the density matrix embedding theory (DMET) and its spectral extension[28–33]. At the heart of the embedding procedure lies the Schmidt decomposition of the wave function. Formally, the Schmidt decomposition of a state is given by

$$|\Psi\rangle = \sum_{i,j=1}^{m_\alpha} \lambda_{ij} \, |\alpha_i\rangle \, |\beta_j\rangle \ , \tag{2}$$

where $\{|\alpha\rangle\}$ represent the states that span the part of the system of interest, the fragment and $\{|\beta\rangle\}$ represent the states that span the rest of the system, the bath. m_α is the dimension of the fragment space assumed smaller than the bath. The Schmidt decomposition renders the wavefunction expansion in a compact form. Even for a complex state, only a small number of many-body bath states, $|\beta\rangle$, is required to exactly define $|\Psi\rangle$. The projector $\mathcal{P} = \sum_{ij} |\alpha_i\rangle \, |\beta_j\rangle$ projects the full Hamiltonian onto the basis obtained from the Schmidt decomposition, $H_{\rm emb} = \mathcal{P} H \mathcal{P}$. If $|\Psi\rangle$ were the exact ground state of the system, $H_{\rm emb}$, a much smaller Hamiltonian, would yield the exact ground-state energy. However, this procedure is purely formal as we would need to know the exact ground-state wavefunction from the outset, which is impossible to obtain for large correlated systems.

The mean-field solution for the ground state is the single Slater determinant $|\Phi^{(0)}\rangle$. It's Schmidt decomposition can be obtained from single-particle linear algebra[35, 36] at a cost no greater than the diagonalization of the single-particle Hamiltonian. It has the same form as Eq. 2, where the many-body fragment state $|\alpha\rangle$ is constructed from the single-particle states corresponding to the fragment sites (fragment orbitals). For the case of a Slater determinant, the many-body bath states $|\beta\rangle$ take a particularly simple form[29]. In particular, they are constructed from a single-particle bath state (bath orbital) multiplied by a determinant of core electrons. These core orbitals have no overlap with the fragment space. The details of constructing the single-particle fragment, bath and core orbitals are outlined in Refs. [28–32].

The ground-state embedding approach for SIAM is summarized as follows:

1. First, a restricted Hartree-Fock (RHF) calculation which yields a single Slater determinant, $|\Phi^{(0)}\rangle$, is used as an aprroximate ground-state of the SIAM Hamiltonian.

2. A set of local fragment site(s), which includes the interacting impurity, is chosen. The Schmidt decomposition of $|\Phi^{(0)}\rangle$ is performed. Importantly, this decomposition yields a single-particle basis which is used to construct the interacting embedding Hamiltonian, $H_{\rm emb}$. This can be understood as a simple basis transformation of the full SIAM Hamiltonian from the single-particle fermionic site basis to the single-particle Schmidt basis.

3. $H_{\rm emb}$ is easily diagonalized to obtain an approximate correlated ground state wavefunction, $|\Psi_{\rm emb}\rangle$. All expectation values are calculated using $\langle\Psi_{\rm emb}|\hat{O}|\Psi_{\rm emb}\rangle$.

It is to be noted that $|\Psi_{\rm emb}\rangle$ has the same form as the Schmidt decomposed $|\Phi^{(0)}\rangle$, the only difference being that $|\Psi_{\rm emb}\rangle$ is obtained after including the correlations on the fragment whereas the latter included them in a mean-field way.

For the SIAM, there is no self-consistency as the interactions are localized on the impurity and the bath states made out of the conduction band levels is, by default, noninteracting. At $T = 0$, $\mu = 0$ in the SIAM Hamiltonian in Eq. 1 maintains half-filling on the impurity. Since the two-electron Coulomb term appears only on the impurity in $H_{\rm emb}$, $\mu = 0$ still ensures the required half-filling. In this respect the procedure outlined is a 'single-shot' embedding analogous to the $u = 0$ case discussed in [32].

A translationally invariant system like the Hubbard model can be divided into identical fragments each of which is embedded in its own bath. Once the self-consistency has been achieved, the fragment's contribution to the ground state energy is evaluated. The total ground state energy is a sum of such identical contributions from each of the fragments. For SIAM, a non-translationally invariant system, we have only one fragment which includes the impurity site and its correspond-

ing bath. The contribution of the unentangled core orbitals to the total ground state energy cannot be nelected in this case. Performing DMET with this unique partitioning also results in an approximate correlated wavefunction for the full system which in a 'single-shot' gives variational estimates of the ground state energy.

B. Dynamics

The quantum embedding approach has been generalized to dynamic properties, particularly for the evaluation of bulk spectral functions[33, 37]. Here, we apply the method to evaluate the local density of states (LDOS) for the SIAM and provide extensions to the current formulation. The technique builds on the ground-state formalism where a bath space of frequency-dependent many-body states is constructed by the Schmidt decomposition of the linear response vector given by

$$|\Phi^{(1)}(\omega,\eta_1)\rangle = \frac{1}{\omega-(h-\epsilon_0)+i\eta_1}\hat{V}\,|\Phi^{(0)}\rangle \ , \qquad (3)$$

where h is the single-particle Hamiltonian with ϵ_0 it's ground-state energy. $|\Phi^{(1)}(\omega,\eta_1)\rangle$ can be expressed in a Schmidt decomposed form [33]

$$|\Phi^{(1)}(\omega,\eta_1)\rangle = \sum_{ijm}\lambda_{ij}\hat{A}^{(m)}(\omega,\eta_1)\,|\alpha_i\rangle\,\hat{B}^{(m)}(\omega,\eta_1)\,|\beta_j\rangle \ , \qquad (4)$$

where $\hat{A}^{(m)}(\omega,\eta_1)$ and $\hat{B}^{(m)}(\omega,\eta_1)$ are operators that act on the fragment and bath states, respectively. This defines a frequency-dependent basis and the corresponding projector $|K(\omega,\eta_1)\rangle = \{|\alpha\rangle\}\otimes\{\hat{B}^{(m)}(\omega,\eta_1)\,|\beta\rangle\}$, $\hat{\mathcal{P}} = |K(\omega,\eta_1)\rangle\langle K(\omega,\eta_1)|$.

Defining $\hat{H}'(\omega,\eta_1) = \hat{\mathcal{P}}\left(\hat{H}-E_{gs}\hat{\mathbb{1}}\right)\hat{\mathcal{P}}$, where E_{gs} is the energy corresponding to the frequency-independent ground state $|\Psi_{\rm emb}\rangle$ discussed in the previous section. The approximate embedding Green's function is given by

$$G(\omega,\eta_1,\eta_2) = \langle\Psi_{\rm emb}|\,\hat{X}\frac{1}{\omega-\hat{H}'(\omega,\eta_1)+i\eta_2}\hat{V}\,|\Psi_{\rm emb}\rangle \ , \qquad (5)$$

where $V = c_d^{(\dagger)}$ and $X = V^\dagger$ gives the single-particle impurity Green's function with it's imaginary part as the single-particle density of states, namely

$$A(\omega,\eta_1,\eta_2) = -\frac{1}{\pi}\Im[G(\omega,\eta_1,\eta_2)] \ . \qquad (6)$$

This generates a Lorentzian broadened spectral function dependent on the parameters η_1 and η_2. A common choice is to set $\eta_1 = \eta_2$[20, 33]. This choice might not always be desirable, especially for a discretized SIAM, where appropriate broadening of the peak spectrum leads to better resolution of the spectral function at both high and low energies[34, 38, 39]. This emphasizes the need for a more detailed construction of spectral broadening, as discussed below.

C. Peak spectrum and broadening

The size of the frequency-dependent Schmidt basis generally makes it manageable to perform full exact diagonalization (ED) on $\hat{H}'(\omega,\eta_1)$ giving access to its entire eigen-spectrum. This allows one to express Eq.5 in an explicit Lehmann representation. Since the functional form of the eigenvectors, $|\Psi'_n(\omega,\eta_1)\rangle$ and the eigenvalues $E'_n(\omega,\eta_1)$ of $\hat{H}'(\omega,\eta_1)$ are not known, η_1 is chosen to be very small to obtain results independent of it. The value of η_1 determines the number of delta peaks observed when calculating the peak spectrum under the following guideline. Hence, for all the results in Sec.III B, we have used $\eta_1 = 10^{-8}$ which ensured the convergence of the number of delta peaks. The single-particle Green's function is given by

$$G(\omega,\eta_2) = \sum_n \frac{|\,\langle\Psi'_n(\omega)|c_d^\dagger|\Psi_{\rm emb}\rangle\,|^2}{\omega-E'_n(\omega)+i\eta_2} \ , \qquad (7)$$

where we have used

$$\hat{H}'(\omega) = \sum_n E'_n(\omega)\,|\Psi'_n(\omega)\rangle\langle\Psi'_n(\omega)| \ . \qquad (8)$$

If $\omega - E'_n(\omega) = 0$ has m solutions given by $\omega_m^{(n)}$, the denominator of the imaginary part of $G(\omega,\eta_2)$ in Eq.7 can be approximated using a Taylor series around $\omega_m^{(n)}$ up to second order in ω. Integrating over all frequencies gives the spectral function in terms of delta funtions at the peak positions and it's corresponding weights,

$$A(\omega) = \sum_{mn} A_{mn}\delta(\omega-\omega_m^{(n)}) \ , \qquad (9)$$

and the spectral weight is given by

$$A_{mn} = \frac{|C_n(\omega_m^{(n)})|^2}{\left|1-\frac{dE'_n\left(\omega_m^{(n)}\right)}{d\omega}\right|} \ , \qquad (10)$$

where $|C_n(\omega)|^2 = |\,\langle\Psi'_n(\omega)|c_d^\dagger|\Psi_{\rm emb}\rangle\,|^2$. The peak spectrum is convoluted with a Gaussian kernel[20, 38, 39]

$$K(\omega,\omega') = \frac{1}{b\sqrt{\pi}}\exp\left[-(\omega-\omega')^2/b^2\right] \ . \qquad (11)$$

The width, b is chosen to be frequency dependent [20, 34] and of the form

$$b = c_1\omega_{\rm min} + c_2|\omega'| \ , \qquad (12)$$

where $\omega_{\rm min}$ is the position of the lowest lying peak above the fermi energy, and c_1 and c_2 are positive constants. We delay our discussion on how to appropriately choose these constants until Sec.III B. The smooth spectral function is then given by

$$A(\omega) = \int_{-\infty}^{\infty} K(\omega,\omega')A(\omega') \qquad (13)$$

$$\sum_{mn}\frac{A_{mn}}{b\sqrt{\pi}}\exp\left[-(\omega-\omega_m^{(n)})^2/b^2(\omega_m^{(n)})\right] \ , (14)$$

with A_{mn} obtained from Eq.10.

D. Comparison to numerical renormalization-group methods

Since the first applications to the SIAM[40], non-perturbative approaches like the numerical renormalization-group method(NRG)[41] have been successful in descibing both static thermodynamic properties and dynamical response and spectral functions[3, 38]. These approaches have seen the introduction of a variety of techniques aimed at improving accuracy and resolution in both the high and low frequency regions [34, 38]. NRG relies on a logarithmic discretization of the infinite conduction band which maps the Hamiltonian of Eq.1 onto a chain geometry. The mapping is analytically performed with the energy levels of the conduction band arranged according to $\epsilon_n = \pm D\Lambda^{-n}$, where D is the conduction band edge and $\Lambda > 1$ is the discretization parameter. The mapping is exact in the limit $\Lambda \to 1$. For a conduction band with constant hybridization $V_k = V$ and a flat density of states $\rho(\omega) = \sum_k \delta(\omega - \epsilon_k) = 1/2D$ for $\omega \in [D, D]$, the mapping leads to the chain Hamiltonian[41]

$$H = \sum_\sigma \left(\epsilon_d + \frac{U}{2}\hat{n}_{d-\sigma}\right)\hat{n}_{d\sigma} + V\sum_\sigma \left(c^\dagger_{d\sigma}c_{1\sigma} + \text{H.c}\right) + \sum_{\sigma,n=1}^{\infty} t_n \left(c^\dagger_{n\sigma}c_{n+1\sigma} + \text{H.c}\right) \ , \quad (15)$$

with $\Gamma = \pi V^2\rho(0)$ and

$$t_n = \frac{D\Lambda^{-n/2}\left(1+\Lambda^{-1}\right)\left(1-\Lambda^{-n-1}\right)}{\left(2\sqrt{\left(1-\Lambda^{-2n-1}\right)\left(1-\Lambda^{-2n-3}\right)}\right)} \ . \quad (16)$$

In NRG, the Hamiltonian in Eq.15 is iteratively diagonalized increasing the number of sites from the impurity at each iteration and truncating the high-energy states if the number of states in the Fock space exceeds a certain chosen limit. More recent methods such as DMRG and related approaches[19, 42] avoid this iterative procedure by truncating the one-dimensional infinite chain in Eq.15 at a finite length, N and solving for it's ground-state directly. DMRG-like methods allow for an arbitrary discretization of the conduction band. This has the advantage of improving the spectral resolution at high energies by incoporating a linear discretization instad of a logrithmic one which has fewer states at high energies. In NRG calculations, the discretization parameter ranges from $\Lambda = 1.5$ to 2.5[38]. Lower values of Λ imply that more states are retained in each NRG iteration, making it comptationally challenging with incresing number of iterations. This is not the case for DMRG or MPS-based methods where values as low as $\Lambda = 1.05$ have been used[23]. These advantages of DMRG, however, come at the cost of the loss of direct access to the full spectrum of excited states. The embedding scheme proposed here is similar to DMRG or MPS-like methods in terms of the advantages it bears, but is far simpler. If a logarithmic discretization is employed, although not necessary, the infinite chain in Eq.15 may cut-off at a finite N. The process of obtaining the spectral functions starts with the evaluation of the embedded ground-state. In this work, we have used $N \sim 300$. Such large values can be handled easily because the embedded system that ultimately needs to be fully diagonalized is independent of N, and only depends on the size of the fragment embedded.

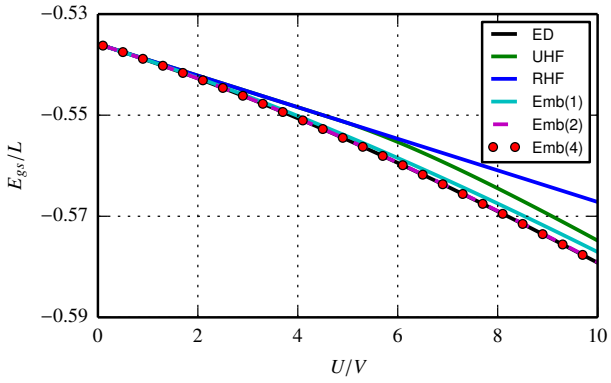

FIG. 1. Ground-state energy per-site E_{gs}/L ($L = 8$) as a function of U for the symmetric SIAM from single-site and cluster embedding. $V_k = V = 0.1$ and Emb(n) referes to the number of sites included in the fragment.

III. RESULTS

A. Finite-sized SIAM

In order to assess the performance of the prescribed embedding method for the SIAM, we first investigate a small-sized system and the results are compared against mean-field approaches like RHF and UHF and exact results obtained from Exact Diagonalization (ED). For this

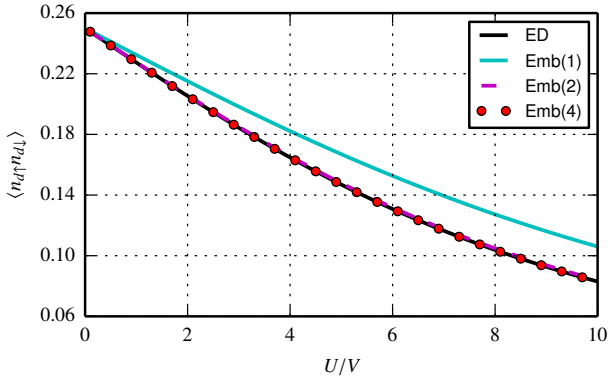

FIG. 2. Double occupany of the impurity $\langle n_{d\uparrow}n_{d\downarrow}\rangle$ for the symmetric SIAM with the same parameters as used in Fig. 1.

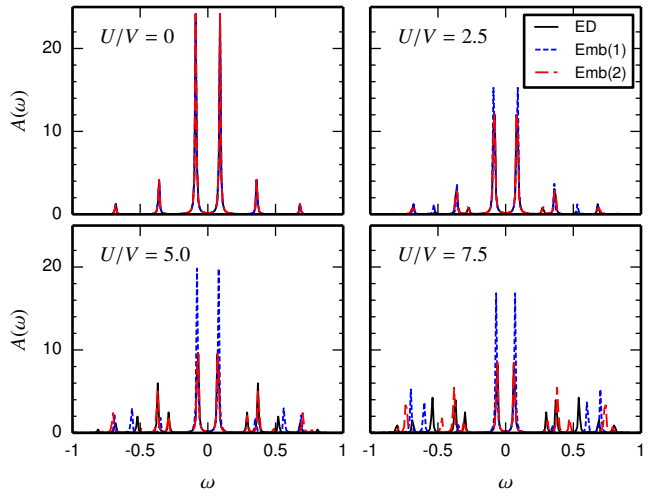

FIG. 3. $T = 0$ single-particle impurity spectral function $A(\omega)$ obtained from one and two-site embedding for the symmetric SIAM with $L = 8$, $V_k = V = 0.1$ and $\eta_1 = \eta_2 = 0.005$ for different interaction strengths.

case, the SIAM is represented by an interacting impurity coupled to seven noninteracting conduction band levels (L=8) at half-filling. We consider the symmetric case with $\epsilon_d = -U/2$. The seven conduction band levels are evenly spaced on $[-1, 1]$. The hybridization energy from the impurity to the conduction band is taken to be same for all the conduction band levels with $V_k = V = 0.1$.

Fig.1 shows the ground-state energy per-site E_{gs}/L as a function of U. The various levels of embedding depend on the number of sites included in the fragment. Emb(n) refers to a fragment with n sites which is coupled to a bath of the same size. The cost amounts to solving a $2n$ sized system which is achieved via ED for small n. For $n = 1$, only the impurity is part of the fragment. For higher values of n, the fragment consists of the impurity and the $n-1$ conduction band levels closest to the fermi energy.

The embedding approach performs better than mean-field methods like RHF and UHF for the entire range of U. This is expected as the embedding improves over RHF by taking into account the interactions on the impurity explicitly. Even Emb(1) which is equivalent to solving a two-site system is significantly better than standard mean-field methods. Higher levels of embedding systematically improve the energies becoming numerically exact when $n = L/2$. This can be seen in Emb(4) which reproduces the ED result at the same cost as doing the ED calculation.

Fig.2 shows the double occupany of the impurity $\langle n_{d\uparrow} n_{d\downarrow} \rangle$ as a function of U. Emb(1) does not capture the correct curvature due to the lack of short-range pairing in the small embedded system. However, cluster embedding generates systematic improvements over the single-site case. Emb(2) is visibly indistinguishable from the exact answer while Emb(4) is numerically exact, as expected.

Fig.3 compares the spectral functions obtained from different levels of embedding approximations with exact results from ED for varying strength of interaction, U. The Lorentzian broadened spectral functions are obtained from Eq.6 with $\eta_1 = \eta_2 = 0.005$. The embedding results are exact in the noninteracting case, as expected, for both single-site and cluster embedding as seen in the top left panel of Fig.3. As U increases the weight of excitations around the Fermi energy decreases and peaks at higher energies are observed. Both Emb(1) and Emb(2) display this general trend. Emb(1) corectly predicts the positions of the low energy excitations but does not accurately reproduce the weight of these excitations. In particular, from $U/V = 2.5$ to $U/V = 5$, Emb(1) incorrectly predicts an increase in the weight of these low-energy excitations around the Fermi energy. This shortcoming as well as the missing details of the high-energy excitations are mostly recovered in Emb(2).

The systematic improvement with cluster embedding and its promising performance on small systems motivates the application of the technique to systems in the thermodynamic limit.

B. Thermodynamic limit

For a single impurity coupled to a continuous conduction band, we take a conduction band with $D = 1$ and use a logarithmic discretization with 299 conduction band states distributed in the interval $[-D, D]$. The discretization parameter is taken as $\Lambda = 1.05$ and the hybridization as $\Gamma = 0.05$. Fig.4 shows the $T = 0$ impurity spectral

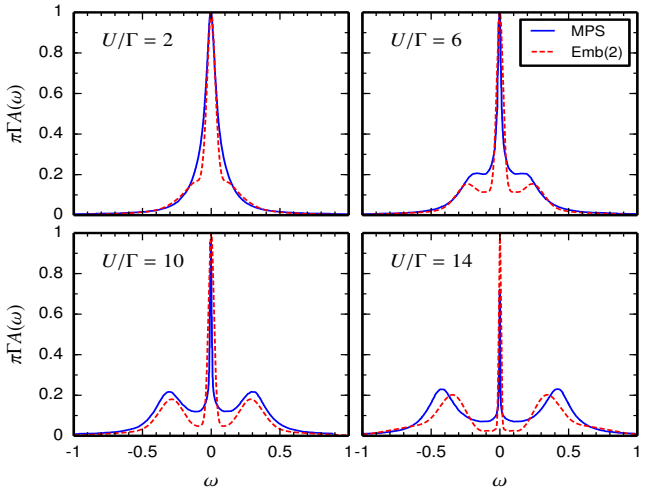

FIG. 4. $T = 0$ impurity spectral function obtained from two-site embedding (dotted line) and Chebyshev-MPS (solid line) for the symmetric SIAM with logarithmically discretized conduction band[23]. The total number of sites in the chain, including the impurity, is 300. $\Lambda = 1.05$, $\Gamma = 0.05$ and $D = 1$. $c_1 \approx 0.3 - 0.4$ and $c_2 \approx 6.8 - 18.8$. The different panels correspond to differnt values of interaction.

function using two-site embedding in the wide-band limit $D \gg \Gamma$, where in each panel we have considered different values of the interaction strength from the weak to strong-coupling regime. Our results are compared to calculations using the Chebyshev-MPS method in the wide-band limit where the computed Chebyshev moments are postprocessed with linear prediction[23]. These results achieve similar precision as the dynamical density matrix renormalization group method(DDMRG)[43] at a lower cost, and serves as a good benchmark for low-cost embedding methods.

The delta peaks and their corresponding weights are obtained from Eq.9 and Eq.10 respectively. As discussed in Sec.II C, the frequency-dependent Gaussian broadening kernel has two parameters, c_1 and c_2 (see Eq.12). At high values of U, the resolution of the Hubbard satellites is almost entirely governed by c_2 as c_1 primarily affects the low energy resolution. As a result, c_2 is chosen such that for strong interactions the high-energy Hubbard satellites have a width of order 2Γ as predicted from strong-coupling results[3]. $c_2 \approx 0.3$ to 0.4 is sufficient to ensure this. With c_2 fixed for all interactions, c_1 is chosen such that the spectral functions essentially recover the Friedel sum rule, namely $A(0) \simeq 1/\pi\Gamma$.

Fig. 4 shows the transfer of spectral weight from low to high-energies at intermediate to strong interactions which marks the canonical distinct features of the SIAM at strong coupling and $T = 0$, namely the upper and lower Hubbard satellites, and a zero-frequency peak, the Abrikosov-Suhl or Kondo resonance. The width of the Kondo resonance decreases exponentially with increasing interaction. This trend is also qualitatively captured by the two-site embedding as seen in Fig.5 where the region near $\omega = 0$ is combined for all four panels of Fig.4. A close examination of Fig.4 shows that at weak interactions, the embedding method overestimates the transfer of spectral weight from the Kondo resonance to the Hubbard bands. However, this is mostly a broadening artifact as the parameter c_2, which was optimized to resolve the Hubbard bands accurately, now affects the low energy resonance. A larger value of c_2 would remedy this defect. However, this would make the proposed broadening scheme inconsistent. For strong interactions ($U/\Gamma = 14$), the peaks of the Hubbard bands are located at $\omega \approx \pm U/2$ which would appear to produce an improvement over the Chebyshev-MPS results. The typical sharpening of the Kondo resonance is seen in Fig.5, however, the width of the Kondo peak is somewhat overestimated in the intermediate-coupling regime. The height of the Kondo resonance deviates from $1/\pi\Gamma$ by less than 1% for all values of interactions considered.

Fig.6 shows single-site embedding results for the symmetric SIAM with a linearly discretized conduction band where 299 conduction band levels are uniformly distributed in $\omega \in [-D, D]$. We have considered the wide-band limit analogous to previous two-site embedding calculations shown in Fig.4 with $\Gamma = 0.05$ and $D = 1$. With increasing interactions, the narrowing of the Kondo resonance and the appearance of the Hubbard bands is observed. We have used the same broadening scheme to convolute the delta peaks. For the single-site embedding, the narrowing of the Kondo resonance is not as sharp as the two-site case but still follows the correct trend as seen from the inset in Fig.6. For strong interactions ($U/\Gamma = 14$), the Hubbard band peak is located at slightly higher energies than $\pm U/2$, and Friedel sum rule is obeyed with deviations below 1% for all the interactions considered. For the intermediate coupling regime ($U/\Gamma = 6$), the Hubbard bands seem to be slightly overdeveloped. For weak interactions ($U/\Gamma = 2$), how-

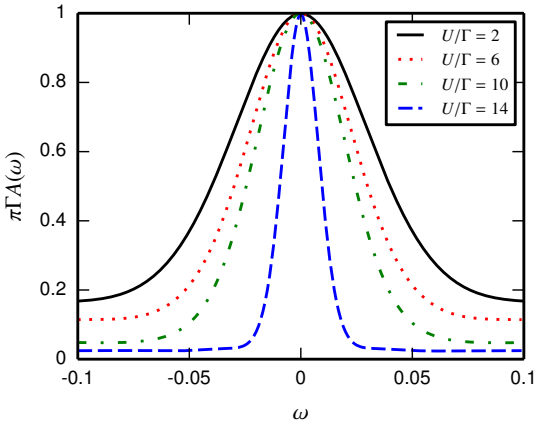

FIG. 5. Narrowing of the Kondo resonance for the spectral functions considered in Fig.4.

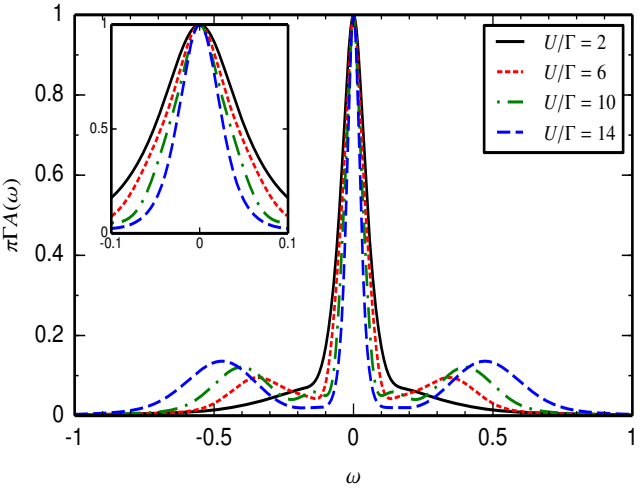

FIG. 6. $T = 0$ impurity spectral function obtained from single-site embedding (Emb(1)) for the symmetric SIAM with a linearly discretized conduction band. 299 conduction band levels are evenly spaced in $\omega \in [-1, 1]$. $\Gamma = 0.05$ and the range of interactions considered is the same as in Fig.4. $c_1 \approx 0.3 - 0.35$ and $c_2 \approx 6.1 - 12.0$. The inset shows the narrowing of the Kondo resonance.

ever, the spectra appears to be more accurate than what was observed for the two-site embedding case.

IV. CONCLUSION

In this work we outline and investigate a very simple embedding approach for calculating the spectral properties of the single impurity Anderson model. The method essentially combines features from density matrix embedding theory (DMET) with discretization and broadening schemes adopted from numerical renomalization group (NRG) approaches. We advocate a 'single-shot' embedding scheme whereby no self-consistency is required, even for cases where multiple bath sites are included in the embedding. The approach provides results compatible with much more advanced DMRG-based algorithms at a fraction of the numerical complexity and expense.

The approach discussed in this work should find useful application as an impurity solver for DMFT, as a prior for analytical continuation of imaginary-time quantum Monte Carlo, and for investigation of the spectral features of more complex impurity problems in their own right. With respect to the latter, it should be noted here that much more complex impurity problems, such as those with multiple orbitals and coupled sites are amenable to the method discussed here with limited additional expense. Future work will be devoted to study of both more complex impurity problems such as multi-orbital cases that emerge in DMFT as well as testing our approach on the more subtle and intricate two-impurity Anderson model.

While this paper was being written we became aware of a related work by Kretchmer and Chan[44]. This works investigates non-equilibrium transport in the Anderson impurity model while we focus, with a slightly different methodology, on the equilibrium spectral properties.

V. ACKNOWLEDGEMENTS

SM thanks Garnet K. Chan for useful discussions. DRR acknowledges funding from NSF CHE-1464802.

[1] U. Weiss, *Quantum Dissipative Systems*.
[2] P. W. Anderson, Phys. Rev. **124**, 41 (1961).
[3] A. C. Hewson, *The Kondo Problem to Heavy Fermions*.
[4] W. Metzner and D. Vollhardt, Phys. Rev. Lett. **62**, 324 (1989).
[5] A. Georges and G. Kotliar, Phys. Rev. B **45**, 6479 (1992).
[6] A. Georges, G. Kotliar, W. Krauth, and M. J. Rozenberg, Rev. Mod. Phys. **68**, 13 (1996).
[7] J. Hubbard, Proc. Roy. Soc. London **A 276**, 238 (1963).
[8] M. C. Gutzwiller, Phys. Rev. Lett. **10**, 159 (1963).
[9] J. Kanamori, Prog. Theor. Phys. **30**, 275 (1963).
[10] Y. Kuramoto, Z. Phys. B **53**, 37 (1983).
[11] N. Grewe, Z. Phys. B **53**, 271 (1983).
[12] N. E. Bickers, Rev. Mod. Phys. **59**, 845 (1987).
[13] T. A. Costi, J. Kroha, and P. Wölfle, Phys. Rev. B **53**, 1850 (1996).
[14] M. Jarrell and J. Gubernatis, Physics Reports **269**, 133 (1996).
[15] A. N. Rubtsov, V. V. Savkin, and A. I. Lichtenstein, Phys. Rev. B **72**, 035122 (2005).
[16] P. Werner, A. Comanac, L. de' Medici, M. Troyer, and A. J. Millis, Phys. Rev. Lett. **97**, 076405 (2006).
[17] E. Gull, A. J. Millis, A. I. Lichtenstein, A. N. Rubtsov, M. Troyer, and P. Werner, Rev. Mod. Phys. **83**, 349 (2011).
[18] A. J. Daley, C. Kollath, U. Schollwck, and G. Vidal, Journal of Statistical Mechanics: Theory and Experiment **2004**, P04005 (2004).
[19] F. Verstraete, V. Murg, and J. Cirac, Advances in Physics **57**, 143 (2008).
[20] R. Peters, Phys. Rev. B **84**, 075139 (2011).
[21] L. Bartosch, H. Freire, J. J. R. Cardenas, and P. Kopietz, Journal of Physics: Condensed Matter **21**, 305602 (2009).
[22] A. Isidori, D. Roosen, L. Bartosch, W. Hofstetter, and P. Kopietz, Phys. Rev. B **81**, 235120 (2010).
[23] M. Ganahl, P. Thunström, F. Verstraete, K. Held, and H. G. Evertz, Phys. Rev. B **90**, 045144 (2014).
[24] F. A. Wolf, J. A. Justiniano, I. P. McCulloch, and U. Schollwöck, Phys. Rev. B **91**, 115144 (2015).
[25] F. A. Wolf, I. P. McCulloch, O. Parcollet, and U. Schollwöck, Phys. Rev. B **90**, 115124 (2014).
[26] M. Ganahl, M. Aichhorn, H. G. Evertz, P. Thunström, K. Held, and F. Verstraete, Phys. Rev. B **92**, 155132 (2015).
[27] F. A. Wolf, A. Go, I. P. McCulloch, A. J. Millis, and U. Schollwöck, Phys. Rev. X **5**, 041032 (2015).
[28] G. Knizia and G. K. Chan, Phys. Rev. Lett. **109**, 186404 (2012).
[29] G. Knizia and G. K. Chan, Journal of Chemical Theory and Computation **9**, 1428 (2013).
[30] I. W. Bulik, G. E. Scuseria, and J. Dukelsky, Phys. Rev. B **89**, 035140 (2014).
[31] I. W. Bulik, W. Chen, and G. E. Scuseria, The Journal of Chemical Physics **141**, 054113 (2014).
[32] S. Wouters, C. A. Jimnez-Hoyos, Q. Sun, and G. K.-L. Chan, Journal of Chemical Theory and Computation **12**, 2706 (2016).
[33] G. H. Booth and G. K.-L. Chan, Phys. Rev. B **91**, 155107 (2015).
[34] A. Freyn and S. Florens, Phys. Rev. B **79**, 121102 (2009).
[35] I. Peschel and V. Eisler, Journal of Physics A: Mathematical and Theoretical **42**, 504003 (2009).
[36] I. Peschel, Brazilian Journal of Physics **42**, 267 (2012).
[37] Q. Chen, G. H. Booth, S. Sharma, G. Knizia, and G. K.-L. Chan, Phys. Rev. B **89**, 165134 (2014).
[38] R. Bulla, T. A. Costi, and T. Pruschke, Rev. Mod. Phys. **80**, 395 (2008).
[39] R. Žitko and T. Pruschke, Phys. Rev. B **79**, 085106 (2009).

[40] H. R. Krishna-murthy, J. W. Wilkins, and K. G. Wilson, Phys. Rev. B **21**, 1003 (1980).
[41] K. G. Wilson, Rev. Mod. Phys. **47**, 773 (1975).
[42] U. Schollwöck, Annals of Physics **326**, 96 (2011).
[43] A. Holzner, A. Weichselbaum, I. P. McCulloch, U. Schollwöck, and J. von Delft, Phys. Rev. B **83**, 195115 (2011).
[44] J. S. Kretchmer and G. K. Chan, arXiv:1609.07678 (2016).